EDGE ARTICLE

Check for updates

Chirality-induced stereoselective synthesis of chiral sp²-carbon-conjugated covalent organic frameworks

Weijun Weng, Zihan Zhu, Xiaoyan Xu and Jia Guo [ID] *

A fully conjugated sp²-carbon covalent organic framework (sp²C-COF) possessing global conformational chirality holds great promise for advanced electronic devices. However, the inherent irreversibility of many reactions hinders the chirality-induced synthesis of COFs from achiral building blocks. Herein, we address a chirality-induced linkage exchange strategy to fabricate a vinylene-linked chiral sp²C-COF *via* an irreversible aldol reaction. The approach involves the pre-synthesis of a chiral Schiff-base precursor, followed by its acid-catalyzed conversion from imine to vinylene linkages. This chiral precursor induces the orientation of asymmetric vinylene linkages, enabling the enantioselective formation of periodic frameworks. Through a self-template mechanism, the layered stacking amplifies the structural chirality and dominates the evolution of branched nanofibers. The resulting chiral sp²C-COF exhibits a high dissymmetry factor in circularly polarized luminescence along with a substantial quantum yield, achieving a superior figure of merit of up to 0.01. An ultrathin film of the chiral sp²C-COF is fabricated and implemented in an interdigitated capacitive sensor capable of the simultaneous quantification and chiral recognition of tryptophan within the 10–40 μM range. This work not only provides a strategic pathway to overcome chiral propagation barriers in irreversible reactions but also introduces an emerging class of chiral two-dimensional carbon materials.

Introduction

Chiral materials have contributed to the advancement of the state-of-the-art technologies relevant to broad fields such as asymmetric catalysis,[1] enantiomer separation,[2] sensing,[3] spintronics and nonlinear optics.[4,5] Carbon materials including fullerenes and carbon nanotubes exhibit inherent chirality in their structures,[6] allowing an additional control over related properties and thereby increasing their usefulness in potential applications. However, this is not the case for two-dimensional (2D) sp²-carbon systems like graphene, which lack inherent chirality because of their planarity. The introduction of chiral elements into planar carbon nanostructures is still in its infancy and needs to be well explored.

The integration of chirality into 2D carbon nanostructures *via* chemical strategies has primarily relied on the functionalization of planar carbon skeletons, such as graphene, with chiral compounds through either covalent[7,8] or non-covalent coupling routes.[9,10] Although these methods facilitate the bulk preparation of chiral 2D materials, they often result in compromised optoelectronic properties and necessitate precise control over domain sizes and atomic-level structural motifs. In contrast,

State Key Laboratory of Molecular Engineering of Polymers, Department of Macromolecular Science, Fudan University, Shanghai 200433, China. E-mail: guojia@fudan.edu.cn

bottom-up synthetic routes have emerged as a promising alternative, enabling the construction of chiral molecular nanographene embedded with inherent helicene units.[11] However, such syntheses typically lack enantio-specificity, requiring chiral chromatography to obtain an enantiopure product. Although the eclipsed stacking of chiral nanographene has been exploited to achieve enantioenriched assemblies synthetically, successful examples remain scarce.[12] Hence, the enantioselective synthesis of 2D carbon materials with global chirality continues to pose a significant challenge to the chemical community.

Fully conjugated vinylene-linked 2D covalent organic frameworks (sp²C-COFs) have emerged as a highly promising class of crystalline porous materials, consisting of covalently linked carbon frameworks with alternatively repetitive units.[13] Analogous to graphene, these materials have received much attention because their extraordinary properties are promising for numerous applications.[14–16] The crystalline nature of 2D COFs provides a promising platform for achieving inherent chirality as the layered ordered stacking can suppress rapid conformational equilibration and stabilize enantiomerically pure structures. Nevertheless, such frameworks are typically obtained as racemic mixtures.[17] The introduction of an external chiral source offers a viable route to induce specific handedness during crystallization, resulting in homochiral frameworks, a strategy well established in the synthesis of zeolite[18] and metal

organic frameworks.[19,20] Inspired by this approach, chirality-induced covalent chemistry has been utilized to synthesize optically pure COF from achiral building blocks.[21] However, this strategy has been largely restricted to reversible reaction systems, such as aldimine condensations, which allows for dynamic error correction and chiral induction through reversible bond formation.[22] In contrast, the synthesis of sp²C-COFs typically relies on either irreversible aldol reaction or weak reversible Knoevenagel condensation. When monofunctional chiral inducers are introduced into such systems, the absence of dynamic exchange halts the continuous transmission of chiral information. This termination not only impedes effective chirality transfer but also disrupts the progressive crystallization necessary for forming long-range ordered homochiral frameworks.

Herein, we report, for the first time, a chirality-induced synthesis of vinylene-linked chiral 2D COF derived from achiral building blocks *via* an irreversible aldol reaction. To overcome the limitation imposed by reaction irreversibility, we designed a dynamic reaction pathway that enables controlled conversion from imine to vinylene linkages using chiral Schiff-base precursors. This stereoselective step successfully addresses the longstanding challenge of chiral transfer in irreversible systems, thereby facilitating homochiral crystallization. As the framework evolves in 2D plane, it forms periodic hexagonal structures with well-defined planar (Δ)- or (Λ)-conformers, dictated by the chirality-induced orientation of vinylene linkages. Subsequent self-templated parallel stacking results in the assembly of branched nanofiber architectures. The resulting chiral sp²C-COF exhibits high dissymmetry factors and quantum yields, achieving a circularly polarized luminescence (CPL) figure of merit of up to 0.01, which can be ranked among the top of CPL materials. Furthermore, when coated as an ultrathin film onto an interdigitated capacitive sensor, the material enables simultaneous chiral recognition and quantitative detection of chiral analytes *via* capacitive changes. This work not only establishes a stereoselective linkage exchange pathway for the homochiral crystallization of sp²C-COFs but also constitutes an emerging family of chiral 2D carbon materials with promising applications in chiral optics and sensing.

Results and discussion

Synthesis of chiral sp²C-COF

As shown in Scheme 1a, (R/S)-1-phenylethylamine (PEA) serves as a chiral inducer, reacting with C_3-symmetric aldehyde monomers to form imine linkages. Reversible aldimine condensation facilitates the dynamic exchange of (R/S)-1-PEA with C_2-symmetric amine monomers, resulting in the evolution of a chiral hexagonal framework featured with oriented imine linkages. Using an identical chiral-induced approach, (R/S)-2-phenylpropanal is reacted with 2,4,6-trimethyl-1,3,5-triazine (TMT) *via* the aldol reaction pathway. However, the dynamic exchange between chiral inducers and C_2-symmetric aldehyde monomers is halted due to the irreversible nature of the aldol reaction. Experimental observations indicated that the reaction solution remained transparent and did not generate solid
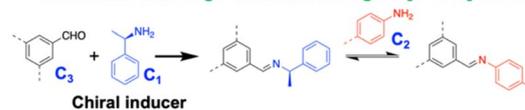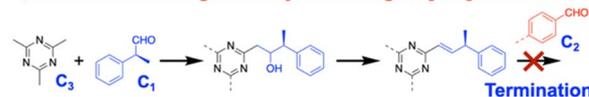

Scheme 1 (a) Previously reported chirality-induced transamination *via* a reversible aldimine condensation reaction. (b) Currently used chirality-induced imine-to-vinylene conversion *via* an irreversible aldol condensation reaction. Reaction conditions: 60 °C, 7 days, CF_3SO_3H (catalyst), mesitylene/dioxane (1/1, v/v).

products. This contrast evidences the challenges associated with chirality-induced synthesis of sp²C-COF. Hence, we address a chirality-induced linkage exchange strategy to overcome this irreversible limitation, successfully incorporating a globally conformational chirality into a high-crystalline 2D sp²C-COF. To redirect the aldol reaction pathway, we initially reacted (R/S)-1-PEA with C_2-symmetric aldehyde monomers to produce imine-linked Schiff-base precursors. This is followed by the aldol reaction with TMT, which enables the stereospecific conversion from imine to vinylene linkages, accompanied by the 2D evolution into hexagonal frameworks based on the C_3-symmetric TMT (Scheme 1b). In the detailed protocol, the imine-to-vinylene linkage transformation proceeded under a solvothermal condition (60 °C for 7 days), with a mixture of mesitylene and dioxane used as a solvent and trifluoromethanesulfonic acid as a catalyst. By altering the reaction temperature and time, appropriate conditions, including moderate temperature (60 °C) and long reaction time (7 days), were found to achieve high yields and optimum chirality (Fig. S1 and S2), resulting in optically pure sp²C-COFs consisting of triazine as a knot and aromatic ring as a linker, *i.e.*, TT-COF (phenyl linker) and TB-COF (biphenyl linker). The CD spectra of the two sp²C-COFs displayed mirror images with a pronounced cotton effect in the visible window (Fig. 1a, c and S3), noticeably differing from the racemic analogues and their chiral model compounds that only have a single CD signal at 249 nm (Fig. S4–S6).

The synthesized sp²C-COFs have been validated using a series of molecular spectroscopy techniques. Fourier transform infrared (FT-IR) spectra revealed a vibration band at 1629 cm⁻¹ assignable to the newly formed vinyl stretch,[23–25] while the characteristic C=O band of the aldehyde group at 1697 cm⁻¹ were severely attenuated, manifesting the formation
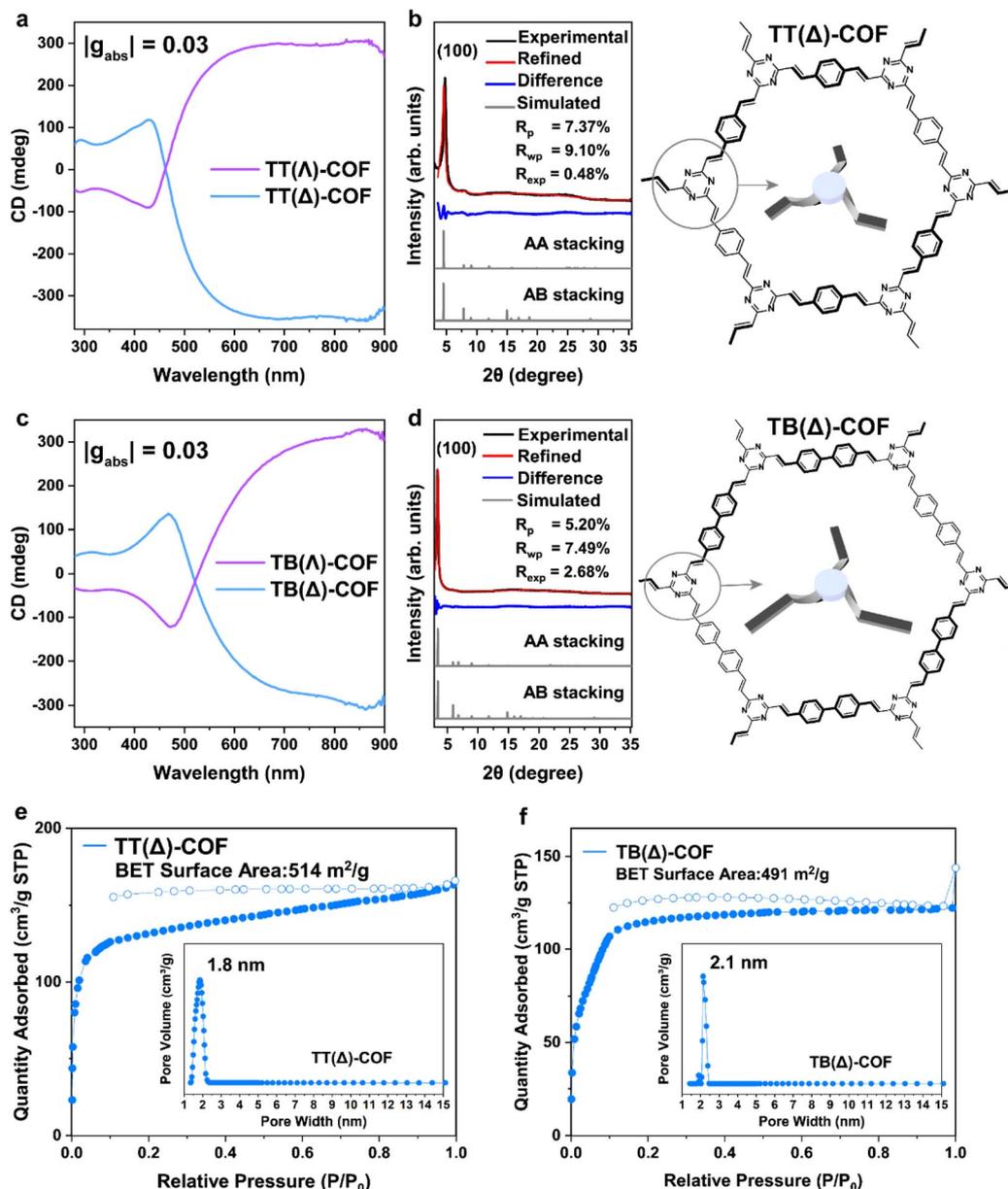
Fig. 1 (a and c) Mirror-imaged CD spectra of chiral TT-COF (a) and chiral TB-COF (c). (b and d) Experimentally obtained WAXS patterns, Rietveld refined patterns, simulated AA and AB stacking patterns and their differences in TT(Δ)-COF (b) and TB(Δ)-COF (d). (e and f) N_2 sorption isotherms of TT(Δ)-COF (e) and TB(Δ)-COF (f). Insets are the pore-size distributions derived from the adsorption curves.

of C=C linkage (Fig. S7). Solid-state cross-polarization magic-angle-spinning ^{13}C NMR spectra showed that the chemical shifts at 138 ppm and 144 ppm corresponded to the newly formed C=C linkage between triazine and phenyl rings, and the multiple overlapped signals from 125 to 132 ppm were attributable to the other carbons of aromatic rings (Fig. S8).[24] To further corroborate the assignment of ^{13}C NMR signals, we synthesized a molecular model compound of sp^{2}C-COFs *via* the aldol reaction between TMT and terephthalaldehyde, which mimics the knot of the sp^{2}C-COF framework by generating three vinylene bonds around the triazine core. The key chemical shifts in the ^{13}C NMR spectrum of this model compound aligned well with those of TT-COF and TB-COF, providing

additional confirmation of the primary repeating unit within the framework. To determine whether (*R*/*S*)-1-PEA remained within the framework, the chiral TT-COF was subjected to strong base digestion to hydrolyze any residual imine linkages. The resulting digestion solution was then analyzed *via* ^1H NMR spectroscopy (Fig. S9). No methyl signals corresponding to (*R*/*S*)-1-PEA were detected, confirming that the chiral inducer was effectively removed during the imine-to-vinylene linkage transformation. This result is consistent with the CD spectroscopy analysis, further supporting the absence of residual chiral inducer in the final product.

The wide-angle X-ray scattering (WAXS) pattern for the chiral sp^{2}C-COF featured the dominated peaks at $2\theta = 4.76°$ for TT-

COF and 3.54° for TB-COF, which were associated with the (100) crystal planes and signified highly ordered 2D periodic frameworks. Refined using the Rietveld method, the reproduced WAXS pattern derived from the AA-stacked models were well in agreement with the experimentally observed patterns with a negligible difference (R_p = 7.37% for TT(Δ)-COF and R_p = 5.20% for TB(Δ)-COF). Thus, as displayed in Fig. 1b and d, we propose that the two COFs crystallize in the hexagonal space group $P6$ with the eclipsed AA-stacking of 2D layers.

Brunauer–Emmett–Teller (BET) surface areas were determined to be 514 and 491 m^2 g^{-1} for TT(Δ)-COF and TB(Δ)-COF, respectively, from N$_2$ sorption measurements at 77 K (Fig. 1e and f). The pore-size distributions were evaluated using the non-local density functional theory, disclosing the uniform pore size of 1.8 nm for TT(Δ)-COF and 2.1 nm for TB(Δ)-COF, in line with those predicted from the AA-stacked COF models. The mirrored COFs offered similar crystalline and porous structures (Fig. S10).

Based on Scherrer's equation, the characteristic X-ray scattering peak of the (100) plane was applied to evaluate the preferential domain size of chiral sp^{2}C-COF. We note that TT(Δ)-COF and TB(Δ)-COF afford the moderate (100) domain sizes of 19.5 and 24.9 nm, respectively. It is likely that the mild reaction conditions retard the crystal growth. Hence, the COF solid was subjected to high-temperature solvothermal treatment (120 °C) for continuous crystallization. After post-ripening, the (100) domain sizes of TT(Δ)-COF and TB(Δ)-COF increased by 13.8% (2.7 nm) and 23.3% (5.8 nm) (Fig. S11, S12a, b and Table S1), respectively, while their BET surface areas increased to 981 and 1483 m^2 g^{-1} (Fig. S12c and d). They also retained consistent signal characteristics in the CD spectra, implying the unchanged chiroptical structure (Fig. S13).

The crystallinity and chiroptical signature of chiral sp^{2}C-COF were preserved even after 24 h of exposure to acidic, alkaline and boiling aqueous conditions (Fig. S14), demonstrating exceptional solvent resistance attributable to its stable parallel stacking structure. It is also noteworthy that the crystallinity of the chiral vinylene-linked sp^{2}C-COF was slightly enhanced after treatment. We attribute this effect to the digestion of amorphous or low-crystalline regions, which increases the relative proportion of highly crystalline domains, a phenomenon consistent with earlier reports on chemically stable sp^{2}C-COF.[23] Therefore, the conformational chiroptical characteristics of sp^{2}C-COF were well maintained even under harsh conditions (Fig. S15).

Insight into the enantioselective synthesis of 2D sp^{2}C-COFs

The aldol condensation can be carried out via the two different routes,[24,25] i.e. a base-catalyzed enolate mechanism and an acid-catalyzed enolic mechanism (Fig. S16), both of which can play a part in the crystallization of sp^{2}C-COFs. Nevertheless, we found that chiral sp^{2}C-COF can only be achieved using an acid catalyst (Fig. S17). To elucidate the acid-catalyzed linkage transformation mechanism, DFT calculation was carried out to reveal the dominant reaction pathway as follows: (1) the single-proton addition on the triazine nitrogen of TMT affords the

enamine form with the electron-rich C=C bond. Note that the formed enamine on the ionized TMT becomes more stable than that on the neutral TMT (Fig. S18). (2) The Schiff-base reaction between (R/S)-1-PEA and 1,4-phthalaldehyde affords the chiral compound with stable trans conformation (Fig. 2a), which can be further protonated in the acidic medium, thereby forming a positively charged nitrogen on the imine bonds. (3) Given that the Schiff-base attracts TMT cations, the unsaturated C=C bond in activated TMT enables addition to the imine carbon of the chiral Schiff-base. Eventually, asymmetric vinyl bonding is formed with the loss of the charged (R/S)-1-PEA.

As aforementioned, the key step in forming the vinylene linkage is the attack of the activated TMT on the trans-form Schiff-base precursor. As illustrated in Fig. 2a, we assume that the group attack involves the frontside and backside pathways. By comparing the transition-state energy barriers (Fig. 2b), the Gibbs free energy of the key intermediate is lower by 5.7 kcal mol^{-1} in the backside pathway than in the frontside pathway, implying the preferential addition of the activated TMT at the back of the Schiff-base precursor. Accordingly, the asymmetric imine direction of the chiral Schiff-base precursor well remains during the imine-to-vinylene transformation through the backside attack, which is opposed to the frontside attack that causes linkage flipping. Such an oriented conformation could be immobilized due to the densely layered stacking during the COF crystallization. We further reason that the Δ conformer of sp^{2}C-COF originates from (R)-1-PEA and Λ from (S)-1-PEA.

Next, we carried out a computational study to understand the origin of the backside attack. Fig. 2b shows the dipole moment of the chiral Schiff-base precursor. The center of the negative charge resides on the backside, manifesting that the ion–dipole interaction determines the direction of the attack. Besides, wave function analysis was used to estimate the additional interaction for the transition complex. Given the independent gradient model based on Hirshfeld partitioning (IGMH), the δg^{inter} index denotes the significance of inter-fragment interaction, and the sign(λ_2)ρ function distinguishes the type and strength of attraction and repulsion.[26] The relation between δg^{inter} and sign(λ_2)ρ is plotted in Fig. 2c, illustrating the weak interaction for the transition complex. The result reveals that the π–π and cation–π interactions assist the addition of the activated TMT. Also, the trans-form chiral Schiff-base precursor can accommodate the electrophilic reagent without steric repulsion.

For comparison, (S)-(+)-3,3-dimethyl-2-butylamine (S-DBA) and (R)-(+)-1-(1-naphthyl)ethylamine (R-NEA) were applied as inducers for the synthesis of chiral sp^{2}C-COFs. Differing from PEA and NEA, the butyl-substituted DBA suffers from the noticeable steric hindrance and in turn suppresses the cation–π interaction within the transition complex. As predicated by the sign(λ_2)ρ function, the DBA-containing transition complex was dominated by the repulsive interaction induced with the steric effect (Fig. S19 and S20). The calculated free energy difference (ΔG) of the key intermediate decreased to 1.9 kcal mol^{-1}, so the stereo- and regio-control of the addition was severely impaired, causing less possibility of formation of oriented vinylene
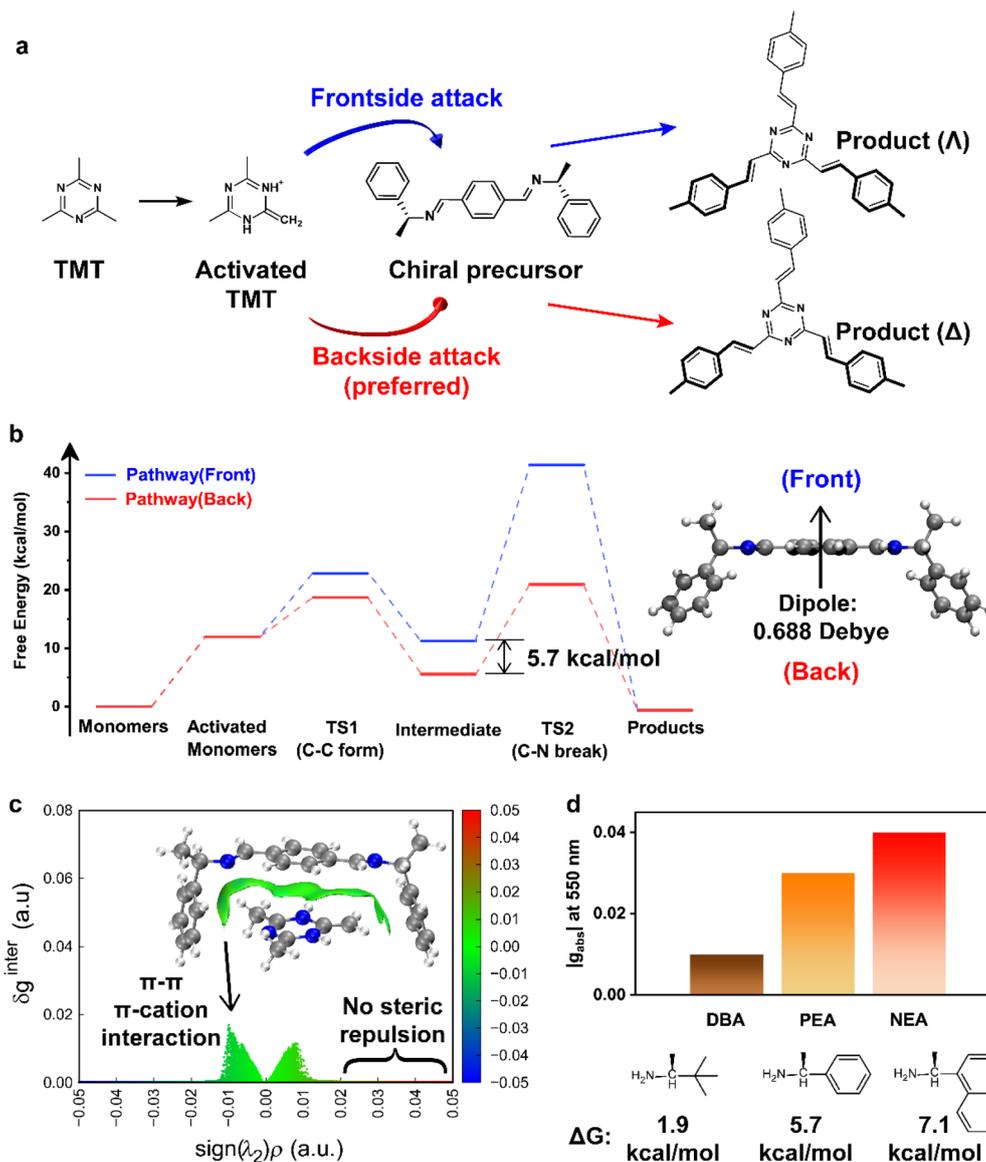
Fig. 2   (a) Illustration of the frontside and backside attack pathways for addition *via* the aldol route. (b) Free-energy diagram of the two pathways for the reaction of activated TMT with the chiral Schiff-base precursor (dipole: 0.688 debye oriented from the back to the front side). (c) IGMH scatterplot of the intermediates (colored by sign(λ_2)ρ function), with the inset of colored real-space presentation (isovalue = 0.005) of the weak interaction *via* IGMH analysis. (d) Asymmetry factor of TT(Δ)-COF synthesized using different chiral amines, with the calculated free-energy difference of the key intermediates.

linkages in the aldol reaction. In contrast, NEA offered the largest ΔG value of 7.1 kcal mol^{-1} compared with the others, indicating the enhanced π–π/cation–π interaction, facilitating stereoselectivity during the imine-to-vinylene conversion.

    The corresponding TT(Δ)-COF was synthesized using *S*-DBA and *R*-NEA as the chiral inducers. The chirality of TT(Δ)-COF(DBA) was inferior to that of TT(Δ)-COFs synthesized by *R*-PEA and *R*-NEA (Fig. 2d), albeit with similar crystallinity (Fig. S21). The result is consistent with the DFT-based inference that enhanced chirality originates from the increased free energy difference of the key intermediate. Hence, both *R*-PEA and *R*-NEA-derived Schiff-base precursors induce the preferred attack pathway by π–π/cation–π interaction and play a key role

in the orientation of vinylene linkages for the chiral sp^{2}C-COF formation.

Chiroptical origin and morphology evolution of sp^{2}C-COF

The chirality-induced linkage exchange ensures the consistent orientation of the three vinylene bonds surrounding the triazine core. The modelling conformation reveals a nonplanar character. The two –C=C– linkages twist to give a small dihedral with the triazine ring, while the third linkage is distorted in the opposite direction (Fig. S22 and Tables S2, S3). The coaxially layered stacking immobilizes the orientation and distortion of the linkages, accordingly maintaining the global conformational chirality.

To shed light on the origin of chiral signals in sp²C-COF, a serial of the cutout models was established *via* a time-dependent DFT calculation. The few-layer (Δ/Λ)-hexagonal macrocycle model exhibits a bisignated CD signal similar to the COF experimental spectra as well as the corresponding rotational strength in the lowest excited state (Fig. S23a and b). The short-wavelength CD signal originates from the vinylene-substituted triazine moiety, and the long-wavelength opposite CD signal originates from the extended framework. As the chiroptical signature is derived from nonorthogonal electric (μ) and magnetic (m) transition dipole moments and directed by the cosine of the angle between μ and m,[27] we studied the transition dipoles of few-layer models (Fig. S23c). It could be inferred that the obtuse and acute angles between μ and m were responsible for the negative cotton effect in the (Δ)-enantiomer and the positive cotton effect in the (Λ)-enantiomer, respectively.

We further investigated how the chiral structure in the sp²C-COF was formed using *in situ* spectroscopic characterizations. As reported earlier, the crystallization of the 2D COFs occurs in three stages: induction, nucleation, and growth.[28] In the initial 30 h, the far-ultraviolet absorbance dramatically dropped, and the absorption edges were gradually red-shifted to around 480 nm (Fig. S24). This implies rapid consumption of monomers to form oligomers that stack together, creating a crystal nucleus.[29] During this period, no CD signals were observed in the visible range. Afterwards, the expansion of crystalline domains was accompanied by an increase in chiral signals. The bisignated CD spectra remained steady after 6 days.

In Fig. 3, the morphology of the chiral sp²C-COF is featured with the tip-ended nanofibers. They gradually evolve through fractal growth, leading to an increase in fibrous branches. A number of flower-like cluster is eventually observed (Fig. S25). We found that the (001) crystal planes of sp²C-COF were parallel to the direction of fiber extension. Additionally, protruding domains appeared on the fibers. A close examination at their edges revealed that the fiber branching was due to the attached domains with layered stacking perpendicular to the fiber surface (Fig. S26). Hence, we assumed that preferential crystallization induces the oriented growth of fibers, while the arbitrary assembling of COF microcrystals is minimal.

Optical circular polarization of chiral sp²C-COFs

To explore the potential of chiral sp²C-COF in the optical circular polarization, an excited-state wavefunction analysis was carried out to visualize the photoelectric behaviors, and the interfragment charge transfer (IFCT) method was used to quantify photoinduced electron accumulation.[30] Real-space representation features a gradient distribution of photoinduced electrons in a planar hexagon model (Fig. S27 and S28). A close observation from the top view revealed that the photoelectron accumulation followed the left-handed gradient in the (Δ)-hexagon and the right-handed gradient in the (Λ)-hexagon, attributable to the chirality-induced spin selectivity (CISS) effect. Accordingly, with the simplified TD-DFT calculation, coaxially stacked multi-layer models allow for top-down photoelectron flowing with the anti-clockwise fluctuation in the (Δ)-macrocycle stacked model and the clockwise fluctuation in the (Λ)-macrocycle stacked model (Fig. S29). All the findings indicate that the structural chirality of sp²C-COFs is characterized by non-axisymmetric lamellar stacking and modulates the spiral-like pathway of photoelectron migration (Fig. S27b).
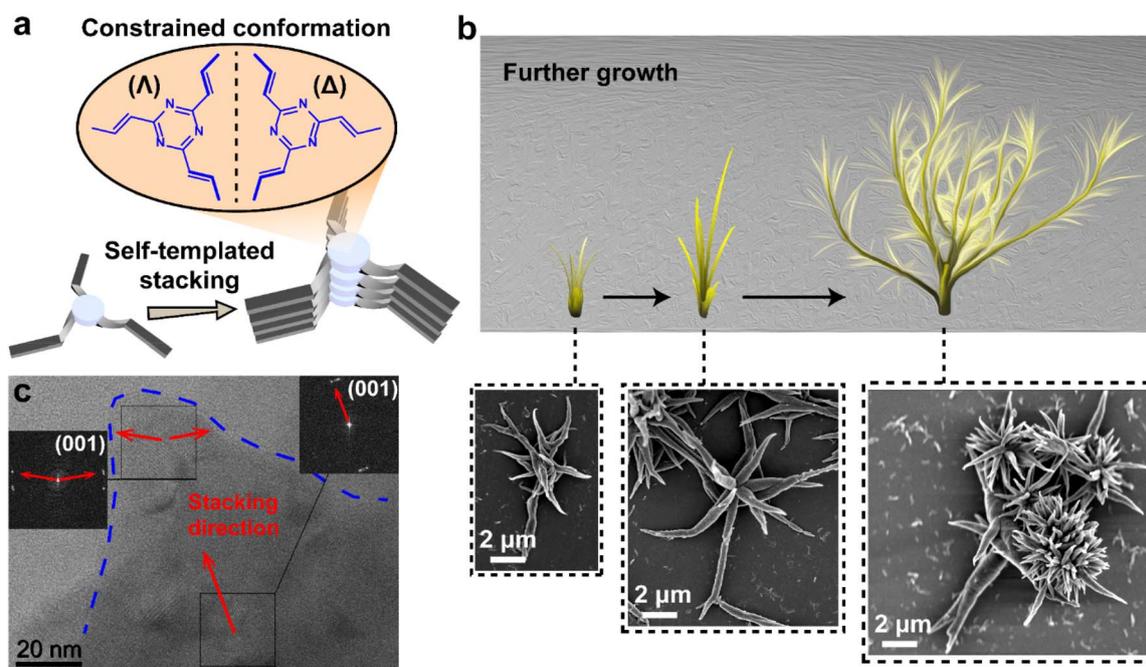

Fig. 3 (a) Illustration of the self-templated crystallization with constrained conformation. (b) Fractal growth of 2D sp²C-COF. (c) HR-TEM image and FFT patterns of the TT(Δ)-COF fiber.

These results suggest the potential for circularly polarized luminescence (CPL) applications of such materials.

Next, we studied the photoluminescence (PL) performance of chiral sp^{2}C-COFs (Fig. S30). The PL spectra of the COF suspensions in glycol were dominated by the green emission centered at 560 nm for TT-COF and 572 nm for TB-COF. The quantum efficiencies of the chiral TT-COF and TB-COF were determined to be 24.7% ± 2.8% and 17.1% ± 0.7%, respectively (Table S4), which were much higher than those of achiral TT-COF (8.0%) and TB-COF (7.3%).

The circularly polarized degree was evaluated by a luminescence asymmetry factor g_{lum},[31] $g_{lum} = 2 \times (I_L - I_R)/(I_R + I_L)$, wherein I_R and I_L are the right- and left-handed PL intensities, respectively. As displayed in Fig. 4a and b, the circularly polarized luminescence (CPL) spectra of the chiral TT-COF and TB-COF give the same negative CPL peaks around 570 nm for the (Δ)-enantiomers and the symmetrical opposite CPL signals for the (Λ)-enantiomers. The CPL signals of the chiral sp^{2}C-COF reached as high as 500 mdeg, and the corresponding $|g_{lum}|$ factors of the emission peaks were calculated to be 0.04 for the chiral TT-COF and 0.06 for the chiral TB-COF (Fig. S31). Accordingly, we calculated the value of figure of merit (FM, FM $= \phi_{PL} \times g_{lum}$) for estimating the overall performance of the chiral sp^{2}C-COFs.[32] TT(Λ)-COF and TB(Λ)-COF afforded FM values of as high as 0.012 and 0.011, respectively, suggesting that this kind of chiral COF can be ranked among the top reported CPL materials (Table S5).

We examined the photophysical process of chiral sp^{2}C-COFs to corroborate their superiority in terms of CPL. Using the time-correlated single-photon counting (TCSPC) technique, the fluorescent lifetimes of the chiral and achiral sp^{2}C-COFs were obtained from the deexcitation process (Fig. S32). The chiral sp^{2}C-COF featured a shorter fluorescence lifetime than the achiral analogues (Fig. 4c), decreasing by 34% for TT-COF and 27% for TB-COF. As is known from the single-crystal data (CCDC 2003349, CCDC 2344737, Fig. 4d), the aldol condensation of TMT with benzaldehyde yields an antiparallel stacking of triphenyl groups instead of layered atomic superimposition, indicating that a more favorable antiparallel stacking sequence exists in the achiral sp^{2}C-COF. In contrast, the chirality-induced orientation of vinylene linkage remains consistent in the whole framework and is immobilized by the layered stacking. Thus, the chiral sp^{2}C-COF tends to adopt the parallel stacking sequence, which has also been evidenced by the earlier reported β-ketoenamine-linked chiral 2D COFs.[33] The parallelly eclipsed stacking alignment may account for the enhanced spontaneous emission rate and, in turn, the reduced fluorescent lifetimes. Indeed, the calculated excitation energy and oscillator strength of the chiral and achiral COF models afforded the spontaneous emission rates of 5.20 and 3.67 μs^{-1}, respectively. The result indicates that rapid deexcitation via radiative transition occurs in the desirable parallel stacking of chiral COF. As fluorescence lifetime is the reciprocal of the spontaneous emission rate, the calculated lifetime of the chiral model was 29% less than that of the corresponding achiral model, which is in good agreement with the experimental results. In addition, the energy bandgap of vertical excitation derived from the TD-DFT calculation was up to 3.74 eV for the parallelly stacked model and 3.39 eV for the antiparallelly stacked model (Fig. S33 and Tables S6, S7). Thus, bandgap broadening also induced a rapid spontaneous
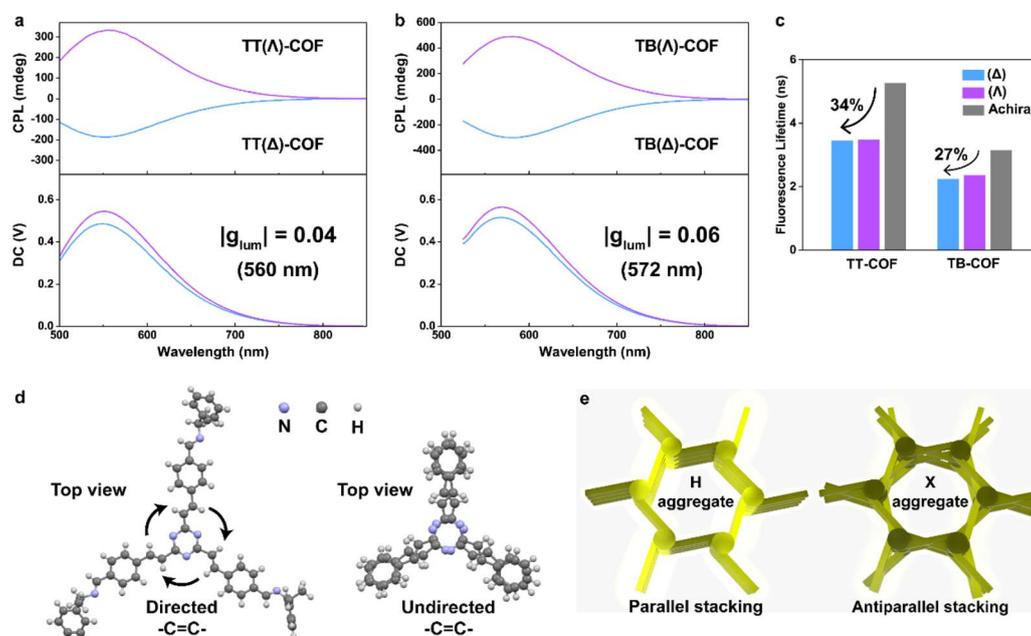

Fig. 4 (a and b) CPL spectra (up) and the corresponding DC curves (bottom) of the mirror-imaged TT-COFs (a) and TB-COFs (b), respectively. (c) Fluorescent lifetime comparison of chiral sp^{2}C-COFs with their achiral analogs. (d) Single crystal structures of the chiral model compound (left, CCDC 2344737) and 2,4,6-tris(2-phenylethenyl)-1,3,5-triazine (right, CCDC 2003349). (e) Illustration of aggregation-induced polarized emission.
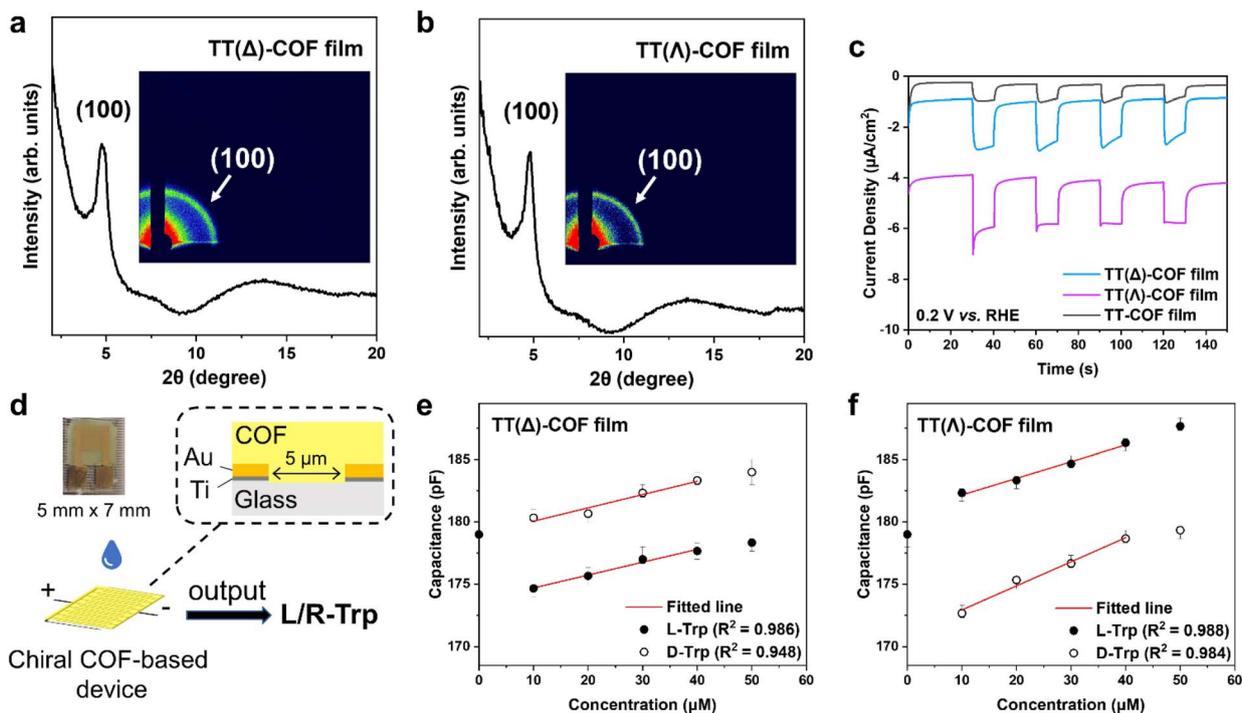
Fig. 5 (a and b) GIWAXS pattern of the TT(Δ)-COF (a) and TT(Λ)-COF films (b). (c) Optoelectrical response of the chiral and achiral TT-COF films. (d) Illustration of the chiral COF-coated IDC sensor for L/D-Trp recognition and detection. (e and f) Capacitance change as a function of Trp concentrations using (e) TT(Δ)-COF- and (f) TT(Λ)-COF-modified IDC sensors, respectively. Insets in (a and b) show the 2D GIWAXS patterns.

emission and improved the fluorescent quantum efficiency of the chiral sp²C-COF.

As illustrated in Fig. 4e, the parallel and antiparallel stacking of chiral and achiral sp²C-COF resembled the H- and X-type aggregations, respectively, both of which can restrict intramolecular rotation and induce excited-state intermolecular charge transfer with reduced excitation energy.[34] As stated by Kasha's theory, only an in-phase dipole arrangement enables electronic excitation of aggregation. The H-aggregation conferred a higher coulomb potential for the in-phase alignment of dipoles than the X-stacking, resulting in a higher excited-state energy with an oscillator strength of $f > 0.01$ (Table S6). In this sense, the chiral sp²C-COF can boost the spontaneous emission rate for the remarkably improved PL efficiency.

With all in mind, we fabricated the optically active PDMS film containing TT(Δ)-COF (Fig. S34). The flexible film maintained its mechanical strength and emitted fluorescence derived from the chiral TT(Δ)-COF components under UV irradiation. Upon exposure to the polarized light, the matched chiral film was excited to emit strong fluorescence; otherwise, the fluorescent signal was nearly invisible.

Preparation of chiral sp²C-COF film for the functionalization of interdigitated capacitive sensors

For device applications, continuous chiral sp²C-COF films are essential and demonstrate superior performance over compressed powder wafers. Using the same imine-to-vinylene exchange approach, we fabricated an ultrathin chiral sp²C-

COF film on ITO glass under solvothermal conditions. Grazing-incidence wide-angle X-ray scattering (GIWAXS) analysis validated that the film maintained the predominant (100) crystal plane (Fig. 5a, b and S35), and SEM revealed a uniform thickness of approximately 300 nm (Fig. S36). As displayed in Fig. 5c, both chiral sp²C-COFs exhibit a higher photocurrent response ($\sim$2 μA cm^{-2}) and lower impedance than their achiral analogues under identical conditions (Fig. S37 and S38), likely due to enhanced charge carrier transport from parallel layered stacking. Between the two materials, TT(Δ)/(Λ)-COF afforded lower impedance than TB(Δ)/(Λ)-COF (Table S8), reflecting its superior conductivity for electronic devices.

Interdigitated capacitive sensing operates as a dielectric-based technique that detects changes in local permittivity at high frequencies, allowing for precise quantification of molecular adsorption events occurring on functionalized electrode surfaces. Thus, we adopted an interdigital capacitor (IDC) composed of classic comb-like Au/Ti electrodes with a center-to-center finger spacing of 5 μm. A compact ultrathin film of chiral sp²C-COF was *in situ* prepared on the IDC surface to serve as a sensing layer. Functionalization with chiral COFs introduces dual functionality: size-selective screening through its uniform pore channels and enantioselective recognition *via* its intrinsically chiral framework. This design enables the sensor to selectively detect chiral molecules, such as amino acids.

As a representative model analyte, tryptophan (Trp) was employed for capacitance measurement using the COF-modified IDC sensor, as illustrated in Fig. 5d. The capacitance response was measured using a handheld LCR meter. The

sensor exhibited a linear increase in capacitance with increasing Trp concentration in the range of 10–40 μM, corresponding to a measurable capacitance window of 170–190 pF (Fig. 5e, f and S39). The high reliability of the detection was evidenced by small error margins (<1%), while its high sensitivity was demonstrated by a shift of 1–2 pF per 10 μM change in (L/D)-Trp. Notably, a significant divergence in capacitance was observed between (L/D)-Trp upon binding with the chiral TT-COF layer, demonstrating the capability of the sensor for chiral discrimination. For 10 μM (L/D)-Trp, the TT-COF-based IDC sensors offered a selectivity factor of 2.6. Also, its sensing-regeneration performance remained stable over the five cycles (Tables S9 and S10).

We attribute the sensing mechanism to the alteration of the local dielectric environment resulting from the incorporation of (L/D)-Trp molecules within the chiral COF pores. According to the fundamental relationship between capacitance and permittivity, this change enhances the capacitive signal. Furthermore, the steric and chemical complementarity between (L/D)-Trp and the chiral binding sites on the COF facilitates stronger multivalent interactions and higher binding affinity for the preferred enantiomer. This leads to enhanced interface polarization and correspondingly larger capacitive response. In contrast, diastereomeric associations result in minimal adsorption and lower capacitive signals.

Conclusions

In this work, we have demonstrated a stereoselective imine-to-vinylene linkage exchange strategy to synthesize a fully conjugated, vinylene-linked 2D chiral sp^{2}C-COF, stemming from chiral Schiff-base precursors *via* aldol condensation. This approach effectively overcomes the fundamental challenge of chirality transfer in the irreversible reaction for COF crystallization. The resulting frameworks exhibit a well-defined conformational chirality, which is stabilized through vertical stacking into a stereospecific layered architecture. This ordered stacking further dominates fractal growth, leading to the formation of a branched nanofiber morphology. Owing to the fully conjugated skeleton, oriented linkages, and highly ordered layered organization, the chiral sp^{2}C-COF possesses pronounced chiroptical properties. As the photoelectron behaviors are influenced by the remarkable CISS effect, the materials exhibit outstanding CPL performance with luminescence dissymmetry factor $|g_{lum}|$ reaching 0.04 for chiral TT-COF ($\Phi_{PL} = 24.7\% \pm 2.8\%$) and 0.06 for chiral TB-COF ($\Phi_{PL} = 17.1\% \pm 0.7\%$), thereby achieving a high FM of up to 0.01. These exceptional properties are attributed to the H-aggregation-type parallel stacking within the layered structure, which promotes a high-energy excited state and increases the spontaneous emission rate and fluorescence efficiency. Furthermore, we prepared a functional interdigitated capacitive sensor modified with an ultrathin chiral sp^{2}C-COF film, which allows for chiral recognition and quantitative detection of tryptophan within the concentration range of 10–40 μM. Hence, our study establishes a reversible linkage exchange pathway for the homochiral crystallization of sp^{2}C-COFs *via* the aldol condensation route, opening new avenues for the design of chiral 2D carbon materials and advancing their application in chiroptical optics and sensing technologies.

Author contributions

J. G. conceived the research and revised the manuscript. W. W. performed experiments, conducted photoluminescence measurements, performed DFT calculations and wrote the manuscript. Z. Z. prepared the COF samples and assisted in WAXS tests. X. X. performed quantum yield measurements and assisted in device fabrication. All the authors reviewed the manuscript.

Conflicts of interest

There are no conflicts to declare.

Data availability

CCDC 2344737 contains the supplementary crystallographic data for this paper.[35]

The data supporting this article have been included as part of the supplementary information (SI). Supplementary information: experimental details, materials, DFT calculations, NMR, CD and UV-vis spectra, structural and morphological characterizations, reaction mechanism studies, electrochemical characterizations, and photoluminescence performances. See DOI: https://doi.org/10.1039/d5sc09234e.

Acknowledgements

Notes and references

1 D. A. Nagib, M. E. Scott and D. W. C. Macmillan, *J. Am. Chem. Soc.*, 2009, **131**, 10875–10877.
2 X. Ye, J. Cui, B. Li, N. Li, R. Wang, Z. Yan, J. Tan, J. Zhang and X. Wan, *Nat. Commun.*, 2019, **10**, 1964.
3 L. Zhang, H. Wang, S. Li and M. Liu, *Chem. Soc. Rev.*, 2020, **49**, 9095–9120.
4 S. Cai, Y. Huang, S. Xie, S. Wang, Y. Guan, X. Wan and J. Zhang, *Angew. Chem., Int. Ed.*, 2022, **61**, e202214293.
5 R. Naaman, Y. Paltiel and D. H. Waldeck, *Acc. Chem. Res.*, 2020, **53**, 2659–2667.
6 M. F. Jesús, J. E. Paul, F. Salvatore, Á. H. María and M. Nazarui, *Acc. Chem. Res.*, 2019, **52**, 1565–1574.
7 X. Zhao, S. Q. Zang and X. Chen, *Chem. Soc. Rev.*, 2020, **49**, 2481–2503.
8 B. Zhao, S. Yang, J. Deng and K. Pan, *Adv. Sci.*, 2021, **8**, 2003681.
9 G. Zhao and H. Zhu, *Adv. Mater.*, 2020, **32**, 1905756.
10 J. Fan and N. A. Kotov, *Adv. Mater.*, 2020, **32**, 1906738.
11 Y. Shen and C. Chen, *Chem. Rev.*, 2012, **112**, 1463–1535.

12 T. Fujikawa, Y. Segawa and K. Itami, *J. Am. Chem. Soc.*, 2015, **137**, 7763–7768.

13 K. T. Tan, S. Ghosh, Z. Wang, F. Wen, D. Rodríguez-San-Miguel, J. Feng, N. Huang, W. Wang, F. Zamora, X. Feng, A. Thomas and D. Jiang, *Nat. Rev. Methods Primers*, 2023, **3**, 1.

14 S. Wei, F. Zhang, W. Zhang, P. Qiang, K. Yu, X. Fu, D. Wu, S. Bi and F. Zhang, *J. Am. Chem. Soc.*, 2019, **141**, 14272–14279.

15 J. Xu, Y. He, S. Bi, M. Wang, P. Yang, D. Wu, J. Wang and F. Zhang, *Angew. Chem., Int. Ed.*, 2019, **58**, 12065–12069.

16 E. Jin, M. Asada, Q. Xu, S. Dalapati, M. A. Addicoat, M. A. Brady, H. Xu, T. Nakamura, T. Heine, Q. Chen and D. Jiang, *Science*, 2017, **357**, 673–676.

17 Y. Hu, S. J. Teat, W. Gong, Z. Zhou, Y. Jin, H. Chen, J. Wu, Y. Cui, T. Jiang, X. Cheng and W. Zhang, *Nat. Chem.*, 2021, **13**, 660–665.

18 J. Li, A. Corma and J. Yu, *Chem. Soc. Rev.*, 2015, **44**, 7112–7127.

19 J. Dong, V. Wee and D. Zhao, *Nat. Mater.*, 2022, **21**, 1334–1340.

20 W. Gong, Z. Chen, J. Dong, Y. Liu and Y. Cui, *Chem. Rev.*, 2022, **122**, 9078–9144.

21 X. Kang, E. R. Stephens, B. M. Spector-Watts, Z. Li, Y. Liu, L. Liu and Y. Cui, *Chem. Sci.*, 2022, **13**, 9811–9832.

22 X. Han, J. Zhang, J. Huang, X. Wu, D. Yuan, Y. Liu and Y. Cui, *Nat. Commun.*, 2018, **9**, 1294.

23 H. Lyu, C. S. Diercks, C. Zhu and O. M. Yaghi, *J. Am. Chem. Soc.*, 2019, **141**, 6848–6852.

24 A. Acharjya, L. Longworth-Dunbar, J. Roeser, P. Pachfule and A. Thomas, *J. Am. Chem. Soc.*, 2020, **142**, 14033–14038.

25 T. Jadhav, Y. Fang, W. Patterson, C. Liu, E. Hamzehpoor and D. F. Perepichka, *Angew. Chem., Int. Ed.*, 2019, **58**, 13753–13757.

26 T. Lu and Q. Chen, *J. Comput. Chem.*, 2022, **43**, 539–555.

27 T. Mori, *Chem. Rev.*, 2021, **121**, 2373–2412.

28 B. J. Smitch and W. R. Dichtel, *J. Am. Chem. Soc.*, 2014, **136**, 8783–8789.

29 H. Li, A. D. Chavez, H. Li, H. Li, W. R. Dichtel and J. Bredas, *J. Am. Chem. Soc.*, 2017, **139**, 16310–16318.

30 Z. Gao, S. Chen, Y. Bai, M. Wang, X. Liu, W. Yang, W. Li, X. Ding and J. Yao, *Phys. Chem. Chem. Phys.*, 2021, **23**, 11548–11556.

31 C. Du, X. Zhu, C. C. Yang and M. H. Liu, *Angew. Chem., Int. Ed.*, 2022, **134**, e202113979.

32 W. Chen, K. Ma, P. Duan, G. Ouyang, X. Zhu, L. Zhang and M. Liu, *Nanoscale*, 2020, **12**, 19497.

33 W. Weng and J. Guo, *Nat. Commun.*, 2022, **13**, 5768.

34 S. Yakali, *Phys. Chem. Chem. Phys.*, 2021, **23**, 11388.

35 CCDC 2344737: Experimental Crystal Structure Determination, 2026, DOI: 10.5517/ccdc.csd.cc2jpwpt.